

Emergent constraints on future precipitation changes

<https://doi.org/10.1038/s41586-021-04310-8>

Hideo Shiogama¹✉, Masahiro Watanabe², Hyungjun Kim^{3,4,5} & Nagio Hirota¹

Received: 17 December 2020

Accepted: 6 December 2021

Published online: 23 February 2022

 Check for updates

Future projections of global mean precipitation change (ΔP) based on Earth-system models have larger uncertainties than projections of global mean temperature changes (ΔT)¹. Although many observational constraints on ΔT have been proposed, constraints on ΔP have not been well studied^{2–5} and are often complicated by the large influence of aerosols on precipitation⁴. Here we show that the upper bound (95th percentile) of ΔP (2051–2100 minus 1851–1900, percentage of the 1980–2014 mean) is lowered from 6.2 per cent to 5.2–5.7 per cent (minimum–maximum range of sensitivity analyses) under a medium greenhouse gas concentration scenario. Our results come from the Coupled Model Intercomparison Project phase 5 and phase 6 ensembles^{6–8}, in which ΔP for 2051–2100 is well correlated with the global mean temperature trends during recent decades after 1980 when global anthropogenic aerosol emissions were nearly constant. ΔP is also significantly correlated with the recent past trends in precipitation when we exclude the tropical land areas with few rain-gauge observations. On the basis of these significant correlations and observed trends, the variance of ΔP is reduced by 8–30 per cent. The observationally constrained ranges of ΔP should provide further reliable information for impact assessments.

Reducing discrepancies (hereafter uncertainty) in climate change projections using Earth-system models (ESMs) is important to inform climate policies, even though ESMs are an ensemble of opportunity and do not necessarily represent the full uncertainties^{9,10}. Emergent constraints (ECs), which consist of statistical (emergent) relationships between aspects of the observable current climate and future change across ESMs, are a promising approach to constrain uncertainties^{2,3}. The uncertainty of future change can be potentially reduced by combining emergent relationships with observations. Statistical relationships alone are not sufficient for convincing ECs—a physically understood mechanism is also needed^{5,11}. There have been large efforts to propose ECs to reduce the uncertainties in the global mean temperature changes (ΔT) (including transient and equilibrium temperature responses to a doubling in carbon dioxide (CO₂) concentration)^{2,3}. In contrast, although the global mean precipitation change (ΔP) provides crucial information as does ΔT (ref. ⁴), to our knowledge, no studies have successfully proposed ECs on ΔP (T and P indicate the global mean temperature and precipitation).

Although long-term historical precipitation change is one of the more obvious candidates for an observable climate metric that might resemble future ΔP , there is a hurdle for ECs. Precipitation is more sensitive to anthropogenic aerosol emissions and volcanic eruptions than to greenhouse gases owing to differences in rapid changes in atmospheric energetics^{4,12}. Historical anthropogenic aerosol emissions and volcanic activities have large effects on past changes in P (refs. ^{13–15}). Therefore, the long-term historical trends of precipitation cannot be

used for the ECs of the future ΔP dominated by responses to greenhouse gas increases (note that aerosol emissions are assumed to be low at the end of the twenty-first century^{16,17}). This is part of the reason why the development of ECs for the future ΔP has not succeeded so far⁴.

In terms of atmospheric energetics, the increased longwave radiative cooling owing to the warming of the troposphere is mainly balanced by increases in the latent heat released by precipitation¹⁸, resulting in a positive ΔT leading to a positive ΔP . As $\Delta P = (dP/dT) \times \Delta T$, ECs on dP/dT (hydrological sensitivity) and/or ΔT could reduce the uncertainty of ΔP . Two studies^{19,20} have proposed ECs on dP/dT based on the Coupled Model Intercomparison Project phase 5 (CMIP5) ensemble⁶, but Pendergrass²¹ found them to be weaker and therefore less useful in the CMIP6 ensemble^{7,8}.

There is a high correlation ($r = 0.83$) between future ΔP and ΔT in the CMIP5 and CMIP6 ensembles (Extended Data Fig. 1, Methods), indicating that the uncertainty of the future ΔP is mainly determined by that of ΔT rather than dP/dT (refs. ^{13,18}). Therefore, even if ECs on dP/dT are not straightforward, there is a possibility of an EC on ΔP owing to the uncertainty reduction of ΔT . Allen and Ingram⁴ tried to constrain the uncertainty of ΔP based on the linear regression between the future ΔP and ΔT and the observationally constrained distribution of future ΔT . However, their constrained range of ΔP was not narrower than the spread of ΔP in a multimodel ensemble because their range of ΔT was broad (1.8–6.5 °C for a doubling of the CO₂ concentration).

Recently, studies of ECs on the future ΔT have found that the influence of aerosols on T trends during recent decades was small owing to the nearly constant global mean aerosol emissions after 1980^{22–25}.

¹Earth System Division, National Institute for Environmental Studies, Tsukuba, Japan. ²Atmosphere and Ocean Research Institute, University of Tokyo, Kashiwa, Japan. ³Moon Soul Graduate School of Future Strategy, Korea Advanced Institute of Science and Technology, Daejeon, Korea. ⁴Dept. of Civil and Environmental Engineering, Korea Advanced Institute of Science and Technology, Daejeon, Korea. ⁵Institute of Industrial Science, University of Tokyo, Tokyo, Japan. [✉]e-mail: shiogama.hideo@nies.go.jp

As both the recent T trends and the future ΔT are mainly driven by greenhouse gas increases, there is a significant positive correlation between the two²³. The emergent relationship between recent past trends and future changes combined with observations suggests that the upper end of the future ΔT across the CMIP5 and CMIP6 ensembles is less reliable and can be reduced (those ESMs with the upper end of the future ΔT overestimate the recent warming)^{23,24,25}. Here we extend this idea of constraints on the future ΔT based on the recent past T trends to ECs on the future ΔP based on the recent past trends of the ΔT . As discussed in the next section, we find significant correlations between the future ΔP and the recent past T trends because there are significant correlations between the future ΔT and the recent past T trends²³ and between the future ΔP and the future ΔT (Extended Data Fig. 1). Narrower ranges of constrained future ΔT based on the abovementioned recent literature than those used in Allen and Ingram⁴ enable us to successfully constrain the future ΔP .

We also examine whether the recent past observed trends of P can be used for ECs on the future ΔP because the aerosol effects on the recent past P trends would be small. As the influences of internal climate variability and uncertainties in the observed data²⁶ are also important issues for ECs, we investigate the influences of these factors on our results.

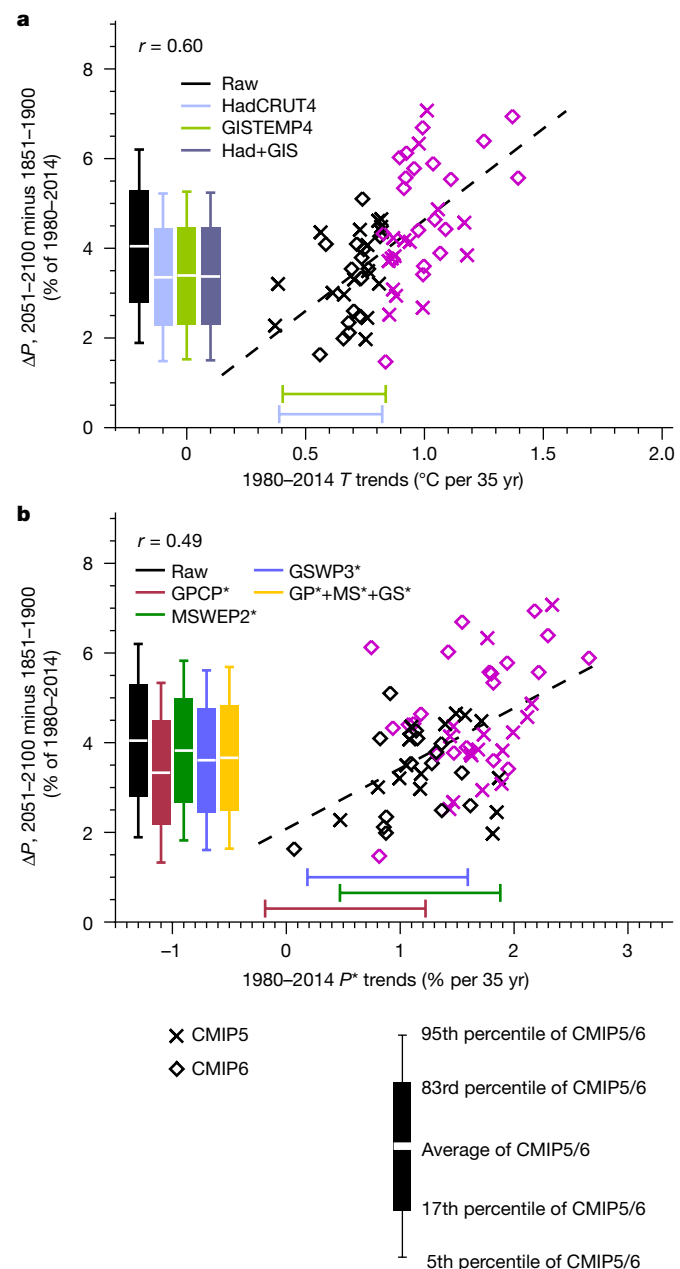
ECs based on recent temperature trends

We mainly analyse the historical and representative concentration pathway 4.5 (RCP4.5)/shared socioeconomic pathway 2-4.5 (SSP2-4.5) simulations (hereafter hist+4.5) of 67 ESMs of the CMIP5⁶ and CMIP6^{7,8} ensembles (Extended Data Table 1, Methods). RCP4.5/SSP2-4.5 represents a medium trajectory for greenhouse gas emissions (low- and high-emission scenarios are investigated in ‘Summary and discussion’). The ensemble average value and the 5–95% range (assuming a Gaussian distribution) of the future ΔP (2051–2100 minus 1851–1900) of hist+4.5 are 4.0% and 1.9–6.2%, respectively. Hereafter, all the precipitation change values are represented as percentages of the 1980–2014 mean values (the period when the observed precipitation datasets are available).

To propose ECs on future projections, it is necessary to identify metrics in past periods that relate well to future changes. We find a statistically significant correlation ($r = 0.60$) between the future ΔP (2051–2100 minus 1851–1900) and the T trends in the recent decades (1980–2014), where the aerosol emission changes were small (Fig. 1a). This relationship suggests that ESMs with larger warming in the recent past tend to simulate greater ΔP in the future.

We apply the hierarchical emergent constraints framework of Bowman et al.²⁷ for ECs (Methods). By comparing the simulated past T trends with observations from Hadley Centre/Climatic Research Unit Temperature version 4 (HadCRUT4)²⁸ (Goddard Institute for Space Studies Surface Temperature Analysis version 4 (GISTEMP4)²⁹), the upper bound (95th percentile value) of the future ΔP is lowered from 6.2% to 5.2% (5.3%) (Fig. 1a, Extended Data Table 2). Here we consider the uncertainty in the internal climate variability by adding linear trends of preindustrial control runs of the ESMs centred around the observed trends. When we take into account the difference between the two observed datasets (Had+GIS), the upper bound becomes 5.2%. The relative reduction of variance (RRV) of the future ΔP (Methods) is 25% for Had+GIS (Extended Data Table 2).

The upper bound of the future ΔP is also lowered when we analyse the T trends of other recent past periods (Extended Data Table 2), which supports the robustness of the results. Although the correlation value between the recent past T trends and the future ΔP is smaller in CMIP5 ($r = 0.44$) than in CMIP6 ($r = 0.69$) because of the lower warming signals^{23–25} and the smaller future ΔP in CMIP5 than in CMIP6, we confirm that ECs using only CMIP5 or CMIP6 lower the upper bounds of the future ΔP (Extended Data Fig. 3).



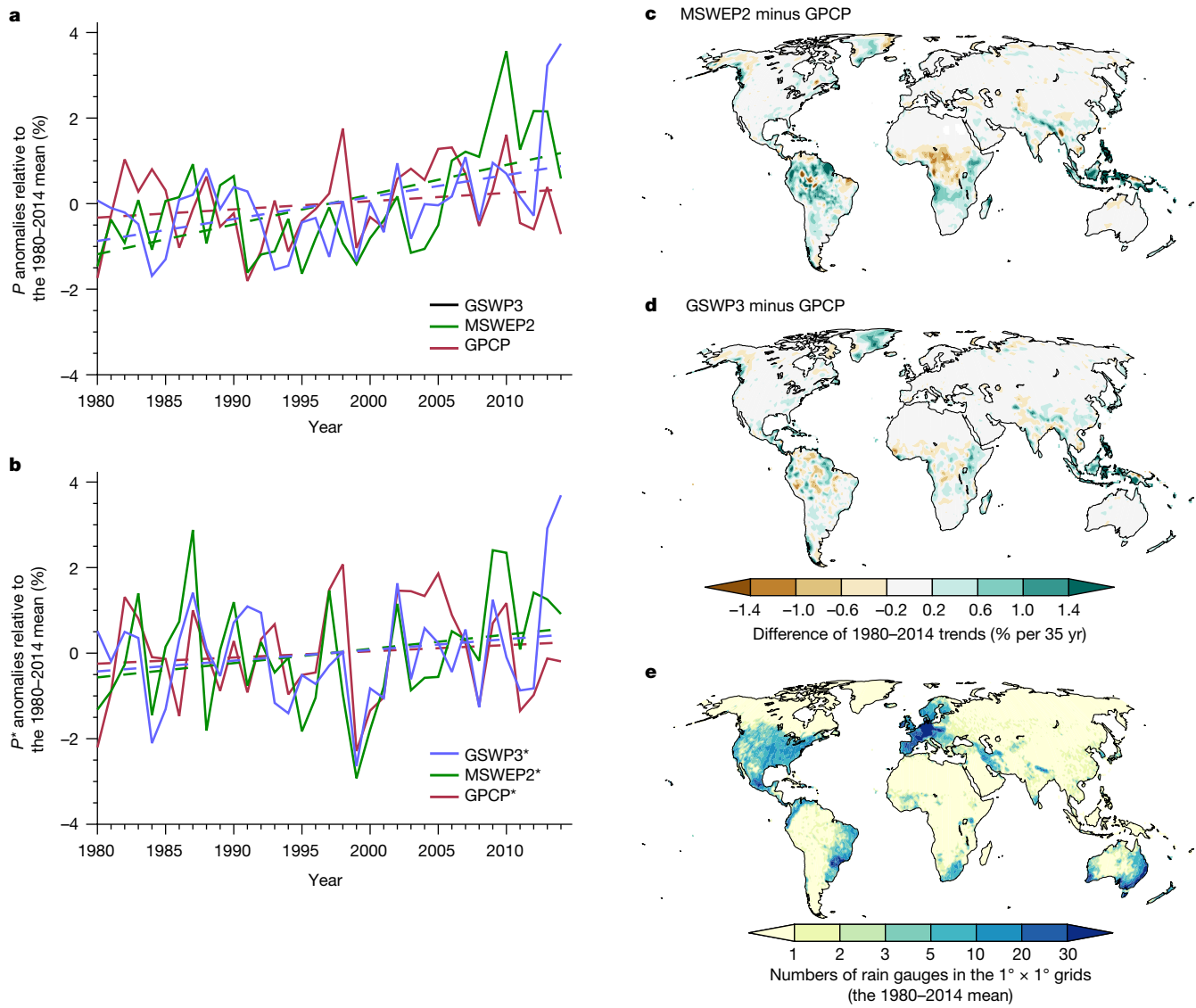


Fig. 2 | Discrepancies between observed precipitation datasets. **a, b**, The solid lines indicate the time series of P (a) and P^* (b) anomalies relative to the 1980–2014 mean (%) of GPCP³⁴ (red), MSWEP2³⁵ (green) and GSWP3³⁶ (blue). P^* is the precipitation averaged over the world except for some tropical land regions with few rain-gauge observations (Extended Data Fig. 2b). The dashed

lines show the linear trends. **c**, Differences in the 1980–2014 precipitation trends (% per 35 yr) between MSWEP2 and GPCP. **d**, The same as c but for GSWP3 minus GPCP. **e**, The 1980–2014 mean numbers of rain gauges in the $1^\circ \times 1^\circ$ grids³⁷ (Methods). Grads was used to draw the maps.

ECs based on recent precipitation trends

We also analyse the separated external forcing experiments of the Detection and Attribution Model Intercomparison Project (DAMIP)^{30,31} of CMIP6 ESMs: well mixed greenhouse gases only (hist-GHG), anthropogenic aerosols only (hist-aer) and natural (solar and volcanic) forcing only (hist-nat) runs. The recent past (1980–2014) trends of P in hist-aer are small, whereas aerosol emissions have large effects on the long-term past (1851–2014) trends^{14,15} (Extended Data Fig. 4). Although volcanic activities affect precipitation for a few years after eruptions^{4,15}, they have a little effect on both the long-term and the recent trends (see hist-nat).

As the recent past P trends in hist+4.5 are dominated by greenhouse gas responses (Extended Data Fig. 4c), the recent past P trends are well correlated with the future ΔP ($r = 0.63$) in CMIP5 and CMIP6 (Extended Data Fig. 5). However, large differences in the P trends among observed datasets^{32,33} prevent meaningful constraints on the future ΔP . We analyse the trends of P derived from Global Precipitation Climatology

Project (GPCP)³⁴, Multi-Source Weighted-Ensemble Precipitation version 2 (MSWEP2)³⁵ and Global Soil Wetness Project Phase 3 (GSWP3)³⁶ (see Methods for the choice of datasets). The upper bound of the future ΔP is lowered (from 6.2% to 4.9%) when we use the 1980–2014 trend of GPCP but not when we use the trends of MSWEP2 (7.1%), GSWP3 (6.3%) or the three observed datasets (GP+MS+GS, 6.2%) (Extended Data Table 2).

The differences between the 1980–2014 P trends in these observed precipitation datasets (Fig. 2a) mainly occur across land rather than ocean (Extended Data Fig. 6). Differences between land precipitation trends are mainly found in some tropical regions where the density of rain-gauge observations³⁷ is generally low (Fig. 2c–e). In these land areas with few rain gauges, precipitation is estimated by combinations of spatial interpolations, satellite measurements, sounding observations and reanalyses^{34–36}, which have many methodological degrees of freedom, leading to large discrepancies in the recent past P trends among these three datasets.

We define P^* as the precipitation averaged over the world except for some tropical ($30^\circ S$ – $30^\circ N$) land regions with fewer than two

rain-gauge observations (Extended Data Fig. 2b, Methods). Differences in the 1980–2014 P^* trends among the three observed datasets are small (Fig. 2b). The 1980–2104 trends of the P and the P^* are well correlated ($r = 0.91$) (Extended Data Fig. 2g). In addition, the 1980–2014 P^* trends are significantly correlated with the future (global mean) ΔP in the ESMs (Fig. 1b). When we use the observed 1980–2014 P^* trends, the upper bound of the future ΔP is lowered from 6.2% to 5.7% for GP+MS+GS (5.3%, 5.8% and 5.6% for GPCP and MSWEP2 and CWP3, respectively) (Extended Data Table 2). The RRV of the future ΔP is 8% for GP+MS+GS.

We confirm that ECs using only CMIP5 or CMIP6 lower the upper bounds of the future ΔP (Extended Data Fig. 3c, d). These results based on the P^* trends of GP+MS+GS are not sensitive to the analysed periods of the recent past trends (Extended Data Table 2). Even if we vary the threshold of rain-gauge numbers between 1 and 3, the upper bounds of the future ΔP are lowered (Extended Data Figs. 2, 7).

We emphasize that the observations of the recent past trends of the T (Fig. 1a) and the P^* (Fig. 1b) consistently suggest reductions in the upper bound of the future ΔP . ESMs with overestimated warming responses to greenhouse gases generally lead to large increases in precipitation during both the recent past and the future periods. Some of the ESMs with larger recent past T trends than that of HadCRUT4 (purple crosses in Fig. 1) also have greater recent past P^* trends than the three observed precipitation datasets and are therefore considered to have low reliabilities in the future projections of ΔT and ΔP .

Spatial distributions of differences

We also investigate the spatial distributions of the differences in the future temperature (Fig. 3a) and precipitation changes (Fig. 3b) between the mean of ESMs with overestimated recent past warming compared with HadCRUT4 (purple symbols in Fig. 1a; overestimated warming models, OWM) and the mean of ESMs whose recent past warming are consistent with HadCRUT4 (consistent warming models, CWM). As expected, there are significant differences in temperature changes in most of the world, with the largest differences found over the northern high latitudes. Significant positive differences in precipitation changes are found, for example, in the northern and southern high-latitude areas, the northeast Pacific Ocean, the central equatorial Pacific Ocean, eastern China, northern Africa and the western Indian Ocean. In these areas, the intermodel correlations between local temperature and precipitation changes in the future are significantly positive (Fig. 3c), which suggests that ESMs with higher warming tend to have greater increases in precipitation owing to thermodynamic changes³⁸. In the Amazon Basin, there are negative precipitation differences between the OWM and the CWM, and significant negative correlations. Dynamical changes in precipitation¹⁰ could lead to this negative difference in precipitation changes.

Summary and discussion

We observationally constrain the uncertainty in the global mean precipitation changes up to the end of the twenty-first century by reducing the confounding influence of anthropogenic aerosols in our analysis. In addition to the constraints of ΔT (refs. ^{23–25}), the upper end of the ΔP in the CMIP5 and CMIP6 ESMs is lowered based on the consistency with the observed datasets: the 95th percentile value of the ΔP up to the end of the twenty-first century is lowered from 6.2% in the raw CMIP5 and CMIP6 ESMs to 5.2–5.7% under the medium greenhouse gas concentration scenario. In this section, the ranges indicate the minimum–maximum values of Extended Data Table 2 using the T trends of Had+GIS and the P^* trends of GP+MS+GS. In contrast, changes in the lower bound (5th percentile) are not robust: the changes are from 1.9% in the raw CMIP5 and CMIP6 ESMs to 1.5–2.0% under the medium greenhouse gas concentration scenario. The variance of the future ΔP is reduced by 8–30%.

Our ECs based on recent T and P^* trends also work well for both the low (RCP2.6 or SSP1-2.6, hist+2.6) and the high (RCP8.5 or SSP5-8.5,

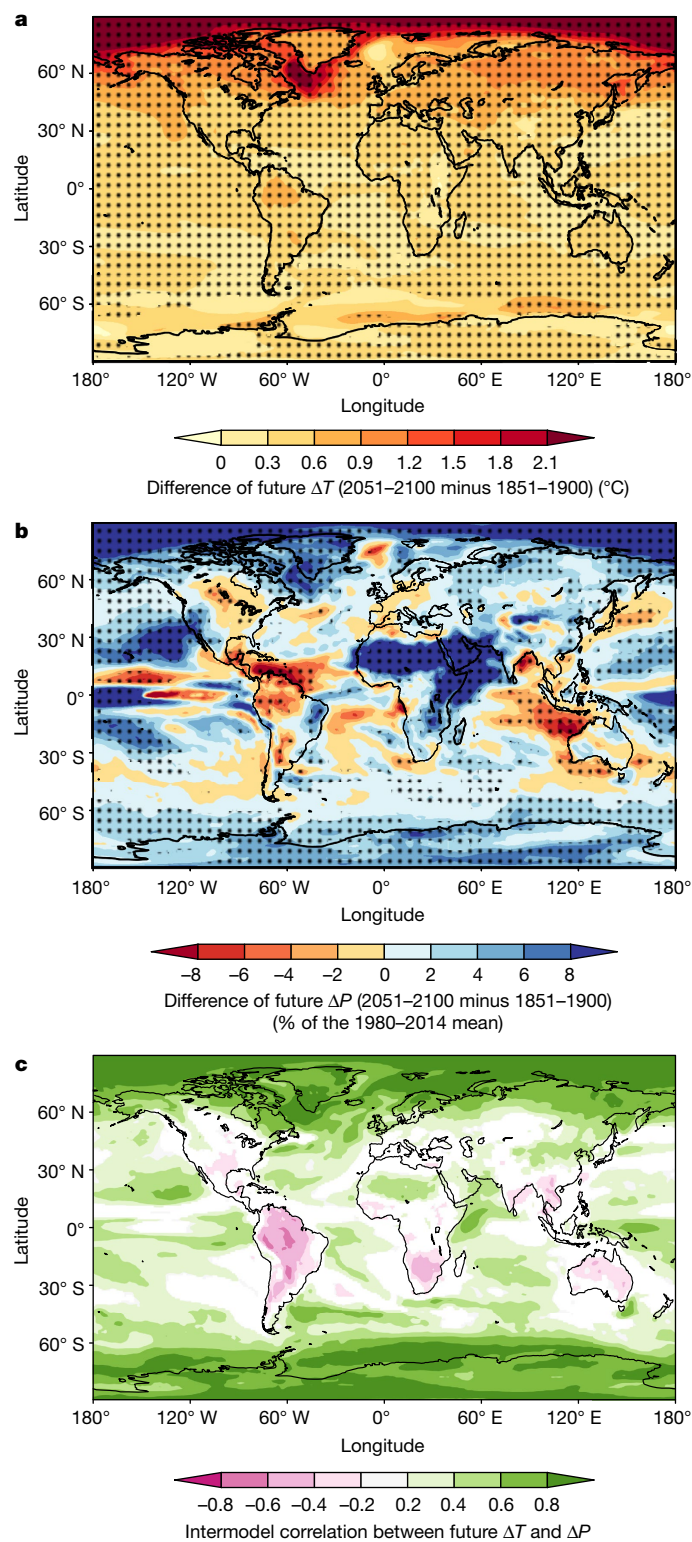


Fig. 3 | Spatial patterns of differences in future temperature and precipitation changes. **a**, Differences in future temperature changes (2051–2100 minus 1851–1900 of hist+4.5, °C) between the OWM and the CWM of CMIP5 and CMIP6^{6–8} (OWM minus CWM). The black hatches indicate that differences are significant at the ±10% level based on Welch's *t*-test. **b**, The same as **a** but for precipitation changes (% of 1980–2014). **c**, Intermodel Pearson's correlations between future temperature and precipitation changes. We draw only correlations that are significant at the ±10% level of the *t*-test. Grads was used to draw the maps.

hist+8.5) greenhouse gas concentration scenarios. The various constraints on the future ΔP suggest reductions in the upper bounds from 5.3% to 4.3–4.9% under hist+2.6 and from 8.6% to 7.4–8.0% under hist+8.5 (Extended Data Table 2). The variances of the future ΔP are reduced by 8–35% under hist+2.6 and 9–27% under hist+8.5 (Extended Data Table 2).

We also discuss the constraints of hydrological sensitivity (dP/dT) (Extended Data Fig. 8). The recent past dP/dT and dP^*/dT are significantly correlated with the future dP/dT ($r = 0.60$ and $r = 0.35$, respectively). However, we cannot constrain the future dP/dT in our approach because the discrepancies among the observed datasets are too large.

Online content

Any methods, additional references, Nature Research reporting summaries, source data, extended data, supplementary information, acknowledgements, peer review information; details of author contributions and competing interests; and statements of data and code availability are available at <https://doi.org/10.1038/s41586-021-04310-8>.

1. Collins, M. et al. in Climate Change 2013: The Physical Science Basis (eds Stocker, T. F. et al.) Ch. 12 (Cambridge Univ. Press, 2013).
2. Hall, A. et al. Progressing emergent constraints on future climate change. *Nat. Clim. Change* **9**, 269–278 (2019).
3. Brent, F. Reducing uncertainties in climate projections with emergent constraints: concepts, examples and prospects. *Adv. Atmos. Sci.* **37**, 1–15 (2020).
4. Allen, M. & Ingram, W. Constraints on future changes in climate and the hydrologic cycle. *Nature* **419**, 228–232 (2002).
5. Schlund, M. et al. Emergent constraints on equilibrium climate sensitivity in CMIP5: do they hold for CMIP6? *Earth Syst. Dyn.* **11**, 1233–1258 (2020).
6. Taylor, K. E., Stouffer, R. J. & Meehl, G. A. An overview of CMIP5 and the experiment design. *Bull. Am. Meteorol. Soc.* **93**, 485–498 (2012).
7. Eyring, V. et al. Overview of the Coupled Model Intercomparison Project phase 6 (CMIP6) experimental design and organization. *Geosci. Model Dev.* **9**, 1937–1958 (2016).
8. O’Neill, B. C. et al. A new scenario framework for climate change research: the concept of shared socioeconomic pathways. *Climatic Change* **122**, 387–400 (2014).
9. Knutti, R. The end of model democracy? *Climatic Change* **102**, 395–404 (2010).
10. Shioigama, H. et al. Observational constraints indicate risk of drying in the Amazon Basin. *Nat. Commun.* **2**, 253 (2011).
11. Caldwell, P. M. et al. Statistical significance of climate sensitivity predictors obtained by data mining. *Geophys. Res. Lett.* **41**, 1803–1808 (2014).
12. Samset, B. H. et al. Fast and slow precipitation responses to individual climate forcers: a PDRMIP multimodel study. *Geophys. Res. Lett.* **43**, 2782–2791 (2016).
13. Thorpe, L. & Andrews, T. The physical drivers of historical and 21st century global precipitation changes. *Environ. Res. Lett.* **9**, 064024 (2014).
14. Salzmann, M. Global warming without global mean precipitation increase? *Sci. Adv.* **2**, e1501572 (2016).
15. Wu, P., Christidis, N. & Stott, P. Anthropogenic impact on Earth’s hydrological cycle. *Nat. Clim. Change* **3**, 807–810 (2013).
16. Rao, S. et al. Future air pollution in the shared socio-economic pathways. *Glob. Environ. Change* **42**, 346–358 (2017).
17. Lund, M. T., Myhre, G. & Samset, B. H. Anthropogenic aerosol forcing under the shared socioeconomic pathways. *Atmos. Chem. Phys.* **19**, 13827–13839 (2019).
18. Fläschner, D., Mauritzen, T. & Stevens, B. Understanding the intermodel spread in global-mean hydrological sensitivity. *J. Clim.* **29**, 801–817 (2016).
19. DeAngelis, A. M., Qu, X., Zelinka, M. D. & Hall, A. An observational radiative constraint on hydrologic cycle intensification. *Nature* **528**, 249–253 (2015).
20. Watanabe, M. et al. Low clouds link equilibrium climate sensitivity to hydrological sensitivity. *Nat. Clim. Change* **8**, 901–906 (2018).
21. Pendergrass, A. G. The global-mean precipitation response to CO_2 -induced warming in CMIP6 models. *Geophys. Res. Lett.* **47**, e2020GL089964 (2020).
22. Jiménez-de-la-Cuesta, D. & Mauritzen, T. Emergent constraints on Earth’s transient and equilibrium response to doubled CO_2 from post-1970s global warming. *Nat. Geosci.* **12**, 902–905 (2019).
23. Tokarska, K. B. et al. Past warming trend constrains future warming in CMIP6 models. *Sci. Adv.* **6**, eaaz9549 (2020).
24. Nijsse, F. J. M. M., Cox, P. M. & Williamson, M. S. Emergent constraints on transient climate response (TCR) and equilibrium climate sensitivity (ECS) from historical warming in CMIP5 and CMIP6 models. *Earth Syst. Dyn.* **11**, 737–750 (2020).
25. Liang, Y., Gillett, N. P. & Monahan, A. H. Climate model projections of 21st century global warming constrained using the observed warming trend. *Geophys. Res. Lett.* **47**, e2019GL086757 (2020).
26. Hegerl, G. C. et al. Challenges in quantifying changes in the global water cycle. *Bull. Am. Meteorol. Soc.* **96**, 1097–1115 (2015).
27. Bowman, K. W., Cressie, N., Qu, X. & Hall, A. A hierarchical statistical framework for emergent constraints: application to snow-albedo feedback. *Geophys. Res. Lett.* **45**, 13050–13059 (2018).
28. Morice, C. P., Kennedy, J. J., Rayner, N. A. & Jones, P. D. Quantifying uncertainties in global and regional temperature change using an ensemble of observational estimates: the HadCRUT4 dataset. *J. Geophys. Res.* **117**, D08101 (2012).
29. Lenssen, N. et al. Improvements in the GISTEMP uncertainty model. *J. Geophys. Res. Atmos.* **124**, 6307–6326 (2019).
30. Gillett, N. P. et al. The Detection and Attribution Model Intercomparison Project (DAMIP v1.0) contribution to CMIP6. *Geosci. Model Dev.* **9**, 3685–3697 (2016).
31. Gillett, N. P. et al. Constraining human contributions to observed warming since preindustrial. *Nat. Clim. Change* **11**, 207–212 (2021).
32. Sun, Q. et al. A review of global precipitation data sets: data sources, estimation, and intercomparisons. *Rev. Geophys.* **56**, 79–107 (2018).
33. Kobayashi, S. et al. The JRA-55 reanalysis: general specifications and basic characteristics. *J. Meteorol. Soc. Jpn.* **93**, 5–48 (2015).
34. Adler, R. et al. The Global Precipitation Climatology Project (GPCP) monthly analysis (new version 2.3) and a review of 2017 global precipitation. *Atmosphere* **9**, 138 (2018).
35. Beck, H. E. et al. MSWEP V2 global 3-hourly 0.1° precipitation: methodology and quantitative assessment. *Bull. Am. Meteorol. Soc.* **100**, 473–500 (2019).
36. van den Hurk, B. et al. LS3MIP (v1.0) contribution to CMIP6: the Land Surface, Snow and Soil moisture Model Intercomparison Project—aims, setup and expected outcome. *Geosci. Model Dev.* **9**, 2809–2832 (2016).
37. Becker, A. et al. A description of the global land-surface precipitation data products of the Global Precipitation Climatology Centre with sample applications including centennial (trend) analysis from 1901–present. *Earth Syst. Sci. Data* **5**, 71–99 (2013).
38. Emori, S. & Brown, S. J. Dynamical and thermodynamic changes in mean and extreme precipitation under changed climate. *Geophys. Res. Lett.* **32**, L17706 (2005).

Publisher’s note Springer Nature remains neutral with regard to jurisdictional claims in published maps and institutional affiliations.

© The Author(s), under exclusive licence to Springer Nature Limited 2022

Methods

ESM simulations

We mainly analyse the historical and RCP4.5/SSP2-4.5 simulations (hist+4.5) of 67 ESMs of the CMIP5⁶ and CMIP6^{7,8} ensembles (Extended Data Table 1). In the historical simulations (1850–2005 for CMIP5 and 1850–2014 for CMIP6), the ESMs are forced by past changes in greenhouse gas concentrations, anthropogenic aerosol emissions, ozone concentration, land use, solar irradiance and volcanic activity. RCP4.5 (2006–2100) and SSP2-4.5 (2015–2100) are scenarios for future changes in greenhouse gas concentrations, anthropogenic aerosol emissions, ozone concentration and land use. SSPS2-4.5 also considers future changes in solar irradiance. In the ‘Summary and discussion’ section, we also analyse the simulations of low (RCP2.6 or SSP1-2.6, hist+2.6) and high (RCP8.5 or SSP5-8.5, hist+8.5) greenhouse gas concentration scenarios.

Estimation of uncertainty ranges

We analyse the averages of the initial-condition ensemble (Extended Data Table 1) for each ESM of CMIP5 and CMIP6. The T trend from HadCRUT4²⁸ is inflated by 1.074 (ref. ²⁵) to convert the observed data of the blended surface air temperature over land and ice and the sea surface temperature over the ocean with limited coverage to the surface air temperature with global coverage. To consider the blending effect, 0.014 °C per decade²³ is added to the temperature trends of GISTEMP4²⁹.

In Fig. 1, to consider the uncertainty of the internal climate variability in the observed trends, we take 500-year data (ten 50-year-length segments) from a pre-industrial control (piControl) run of each ESM (Extended Data Table 1). The number of the piControl segments (N_{pi}) is 520. We add the trend value of each piControl segment to the observed trend and calculate the 5–95% range of the resulting distribution assuming a Gaussian distribution. The standard deviation values of the 35-year (in the case of 1980–2014 analyses) trends of T , P and P^* in all the piControl runs are 0.13 °C, 0.30% and 0.38%, respectively.

The raw 5–95% uncertainty ranges of the future ΔP are estimated by assuming Gaussian distributions of the ESM spreads. We calculate the observationally constrained ranges of the future ΔP by applying the hierarchical emergent constraints framework²⁷. Here, \mathbf{z} and \mathbf{x} are the future changes and the recent trends of ESMs, respectively. μ_z and δ_z are the ensemble mean and standard deviation of \mathbf{z} , respectively. μ_x and δ_x are the ensemble mean and standard deviation of \mathbf{x} , respectively. The correlation between \mathbf{z} and \mathbf{x} is denoted by ρ . When we consider a single observational dataset, \mathbf{y} indicates the vector of the trends of all the piControl segments added to the observed trend (the vector size is N_{pi}). μ_y and δ_y indicate the observed trend (approximately equal to the mean of \mathbf{y}) and the standard deviation of \mathbf{y} , respectively. When we take into account the difference between the multiple observed datasets, \mathbf{y} denotes the vector containing the trends of piControl added to each of the recent trend values of the multiple observed datasets (the vector size is $2N_{\text{pi}}$ for Had+GIS and $3N_{\text{pi}}$ for GP+MS+GS). μ_y and δ_y indicate the mean and standard deviation of \mathbf{y} , respectively.

We estimate the mean ($E(\mathbf{z} | \mathbf{y})$) and standard deviation ($\delta(\mathbf{z} | \mathbf{y})$) of the constrained future projections by the following equations:

$$E(\mathbf{z} | \mathbf{y}) = \mu_z + \frac{\rho \delta_z \delta_x}{\delta_x^2 + \delta_y^2} (\mu_y - \mu_x) \quad (1)$$

$$\delta(\mathbf{z} | \mathbf{y}) = \delta_z \sqrt{1 - \frac{\rho^2}{1 + (\delta_y^2 / \delta_x^2)}} \quad (2)$$

The constrained range of the future ΔP is estimated by assuming a Gaussian distribution with $E(\mathbf{z} | \mathbf{y})$ and $\delta(\mathbf{z} | \mathbf{y})$. The RRV is calculated as follows:

$$\text{RRV} = \left(1 - \frac{\delta^2(\mathbf{z} | \mathbf{y})}{\delta_z^2} \right) \times 100\%. \quad (3)$$

Different observed precipitation datasets

As it is known that there are significant differences in ΔP among observed precipitation datasets, it is important to test the sensitivities of our results to the choice of dataset. There are only a few datasets of observed precipitation that cover the global land and ocean and the 1980 to present period³². We exclude reanalysis datasets, even though they cover this region and time period, because they have artefactual trends owing to temporal changes in assimilated datasets³³. We further exclude the Climate Prediction Center Merged Analysis of Precipitation³⁹ because it has an artefactual decreasing trend in oceanic precipitation owing to input data change⁴⁰. This leaves three datasets: GPCP, MSWEP2(V2.2) and GSWP3. These datasets cover the entire globe and span the period from 1980 to the present. GPCP³⁴ is a merged dataset of gauge stations, satellites and sounding observations and is widely used for climate research. MSWEP2(V2.2) is a newly merged dataset of gauge-, satellite- and reanalysis-based data³⁵. GSWP3 is a merged dataset of dynamically downscaled twentieth-century reanalysis data⁴¹ and global observations of precipitation, temperature and radiation fields^{36,42}.

In Extended Data Fig. 6, we also use the Global Precipitation Climatology Centre (GPCC) land precipitation dataset (full data monthly product version 2020, $1^\circ \times 1^\circ$)^{37,43}. GPCC is derived from quality-controlled station data of rain gauges. Areas without rain-gauge observations were filled by interpolation. Note that GPCC has no data over the Antarctica and ocean areas. GPCC also provides information on the numbers of rain-gauge observations used to calculate each 1×1 grid value of precipitation. We use the numbers of rain-gauge observations of GPCC to calculate ΔP^* (Fig. 2, Extended Data Figs. 2, 3, 7, 8) because the rain-gauge observations involved in GPCP, MSWEP2 and GSWP3 are mainly based on those of GPCC^{34–36}, and these three datasets do not provide information on rain-gauge observation numbers.

Data availability

All data that support the findings of this study are available from the following: CMIP5, <https://esgf-node.llnl.gov/search/cmip5/> (last access, 9 February 2021); CMIP6, <https://esgf-node.llnl.gov/search/cmip6/> (last access, 9 February 2021); HadCRUT4, <https://www.metoffice.gov.uk/hadobs/hadcrut4/> (last access, 7 October 2020); GISTEMP4, <https://data.giss.nasa.gov/gistemp/> (last access, 9 March 2020); MSWEP2 (v2.2), <http://www.gloh2o.org/> (last access, 30 September 2020); GSWP3, http://search.diasjp.net/en/dataset/GSWP3_EXPL_Force (last access, 13 October 2020); GPCC, <https://www.dwd.de/EN/ourservices/gpcc/gpcc.html> (last access, 26 February 2021).

Code availability

The codes are available from <https://doi.org/10.6084/m9.figshare.16816714>.

- 39. Xie, P. & Arkin, P. A. Global precipitation: a 17-year monthly analysis based on gauge observations, satellite estimates, and numerical model outputs. *Bull. Am. Meteorol. Soc.* **78**, 2539–2558 (1997).
- 40. Yin, X. A. & Gruber Arkin, P. Comparison of the GPCP and CMAP merged gauge–satellite monthly precipitation products for the period 1979–2001. *J. Hydrometeorol.* **5**, 1207–1222 (2004).
- 41. Compo, G. P. et al. The Twentieth Century Reanalysis Project. *Q. J. R. Meteorol. Soc. A* **137**, 1–28 (2011).
- 42. Kim, H. *Global Soil Wetness Project Phase 3 atmospheric boundary conditions (experiment 1)* (DIAS, 2017); <https://doi.org/10.20783/DIAS.501>

Article

43. Schneider, U. et al. GPCC Full Data Monthly Product Version 2020 at 1.0°: *Monthly Land-Surface Precipitation from Rain-Gauges Built on GTS-Based and Historical Data* (2020); https://doi.org/10.5676/DWD_GPCC/FD_M_V2020_100

Acknowledgements This work was supported by the Integrated Research Program for Advancing Climate Models (JPMXD0717935457), Grants-in-Aid for Scientific Research (JP21H01161) of the Ministry of Education, Culture, Sports, Science and Technology of Japan, the Environment Research and Technology Development Fund (JPMEERF20202002) and the National Research Foundation of Korea grant (MSIT) (2021H1D3A2A03097768).

Author contributions H.S. mainly performed the analyses and wrote the paper. M.W. provided insights about the physics of precipitation changes and emergent constraints. H.K. provided the GSWP3 data and the information about the uncertainty sources of the observed

precipitation datasets. N.H. contributed to the data collection, the selection of the observed datasets and the interpretation of the results. All authors discussed the results and commented on the manuscript.

Competing interests The authors declare no competing interests.

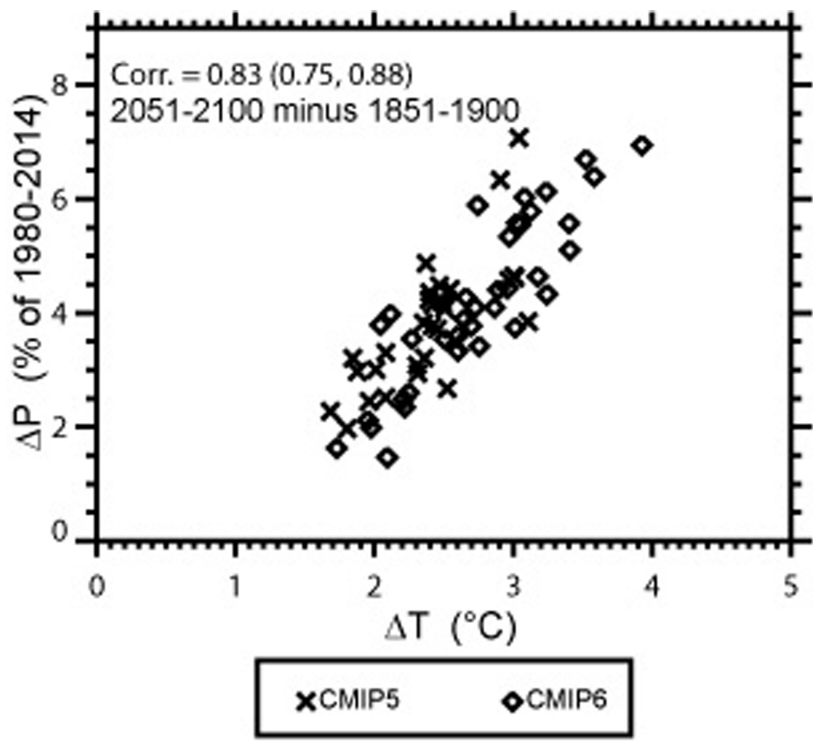
Additional information

Supplementary information The online version contains supplementary material available at <https://doi.org/10.1038/s41586-021-04310-8>.

Correspondence and requests for materials should be addressed to Hideo Shiogama.

Peer review information *Nature* thanks Chad Thackeray, Sabine Undorf and the other, anonymous, reviewer(s) for their contribution to the peer review of this work.

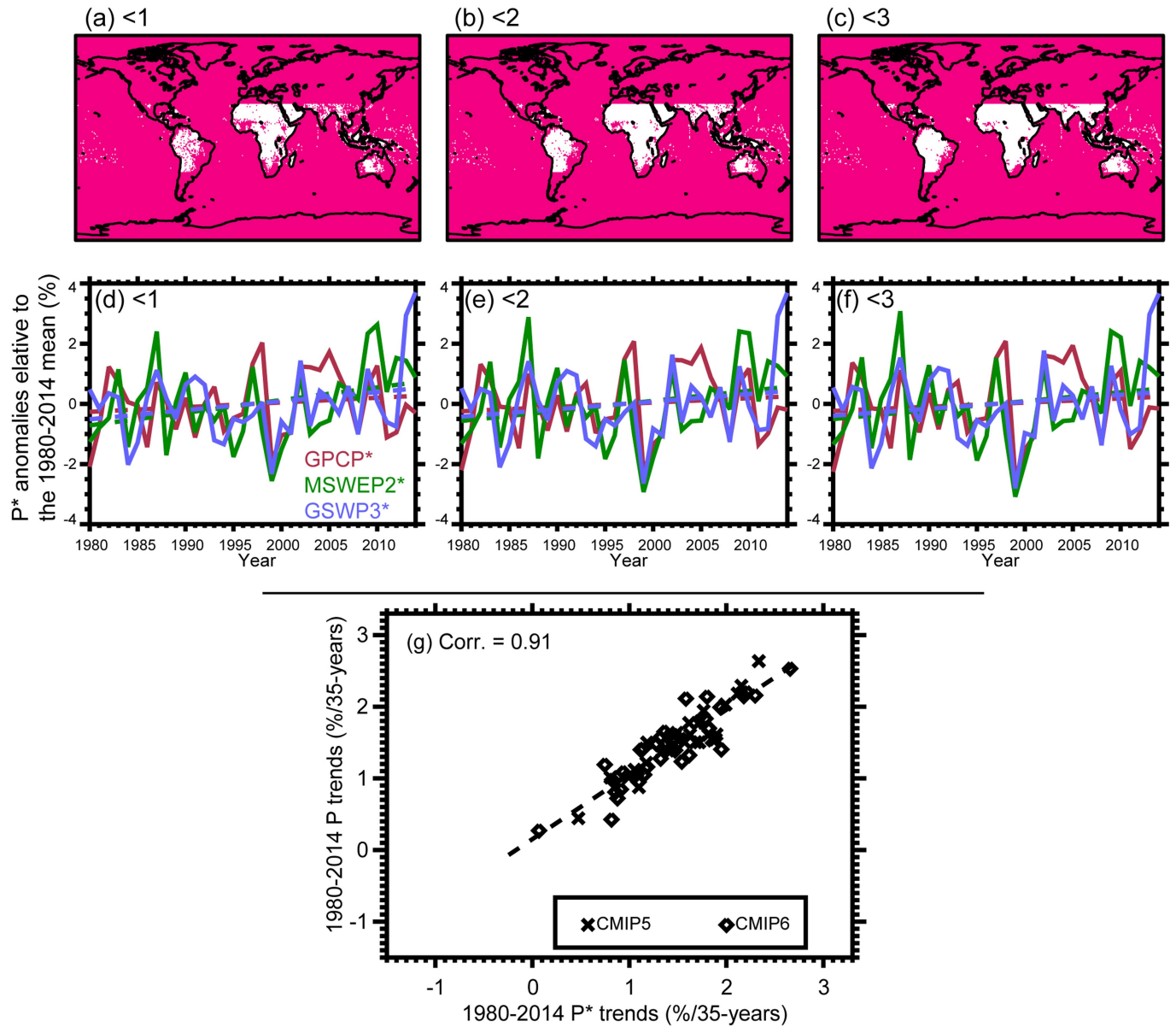
Reprints and permissions information is available at <http://www.nature.com/reprints>.



Extended Data Fig. 1 | Relationships between future ΔT and ΔP . Horizontal and vertical axes indicate the future (2051–2100 minus 1851–1900) ΔT ($^{\circ}\text{C}$) and ΔP (% of the 1980–2014 mean), respectively. Crosses and diamonds are CMIP5

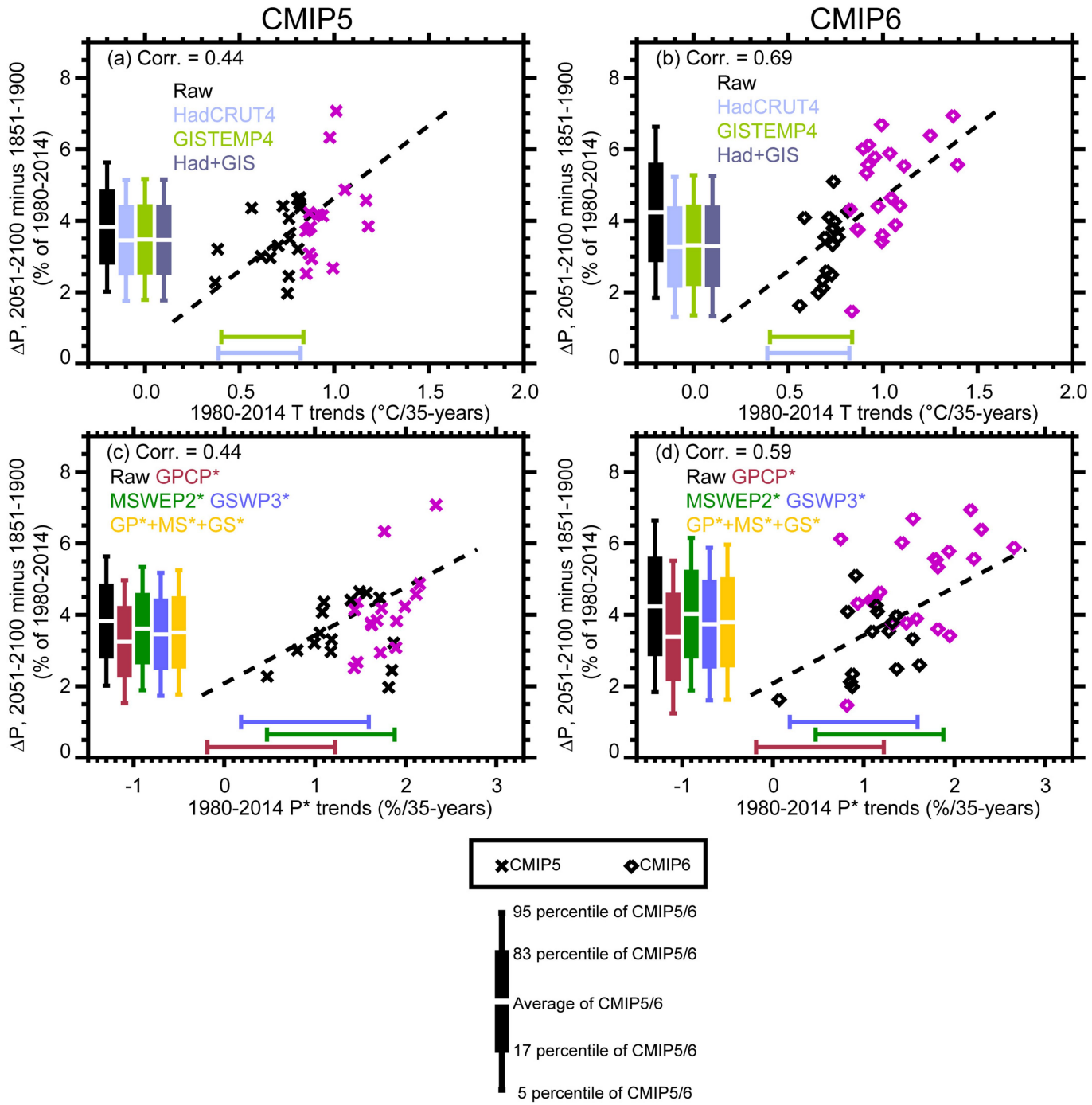
and CMIP6 ESMs (ensemble mean for each ESM), respectively. Pearson's correlations of the CMIP5 and CMIP6 ESMs are denoted in the panel. Those correlations are significant at the 5% level.

Article



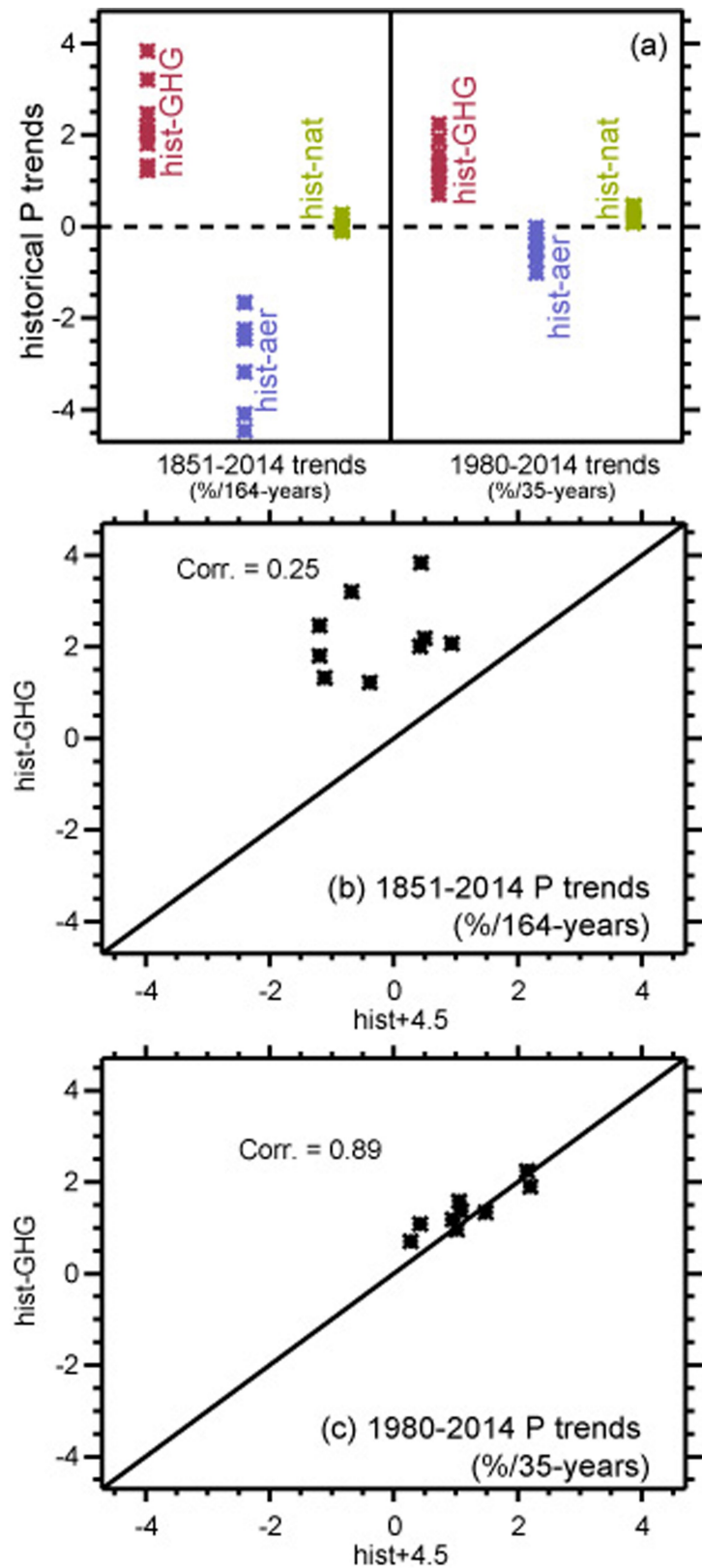
Extended Data Fig. 2 | Definition of P^* . White shaded areas in the top panels indicate tropical ($30^\circ S$ – $30^\circ N$) land regions where 1980–2014 mean numbers of rain gauge observations³⁷ (Methods) are less than (a) 1, (b) 2 and (c) 3. Panels (d), (e) and (f) show P^* anomalies relative to the 1980–2014 mean (%). Here P^* represents the precipitation averaged over the pink shading areas of panels (a), (b) and (c), respectively. Solid lines are GPCP³⁴ (red), MSWEP2³⁵ (green) and GSWP3³⁶ (blue). Dashed lines show their linear trends. Panel (e) is the same as Fig. 2b. We mainly focus on the case of panels (b) and (e) in this paper.

(g) Relationships between the 1980–2014 trends of P and P^* (P^* in the case of (e)). Vertical and horizontal axes indicate the 1980–2014 trends of P and P^* (% per 35 yr), respectively. Crosses and diamonds are CMIP5⁶ and CMIP6^{7,8} ESMs (ensemble mean for each ESM), respectively. Dashed line indicates the linear regression. Pearson's correlation of the CMIP5 and CMIP6 ESMs is denoted in the panel. This correlation is significant at the 5% level. Grads was used to draw the maps.



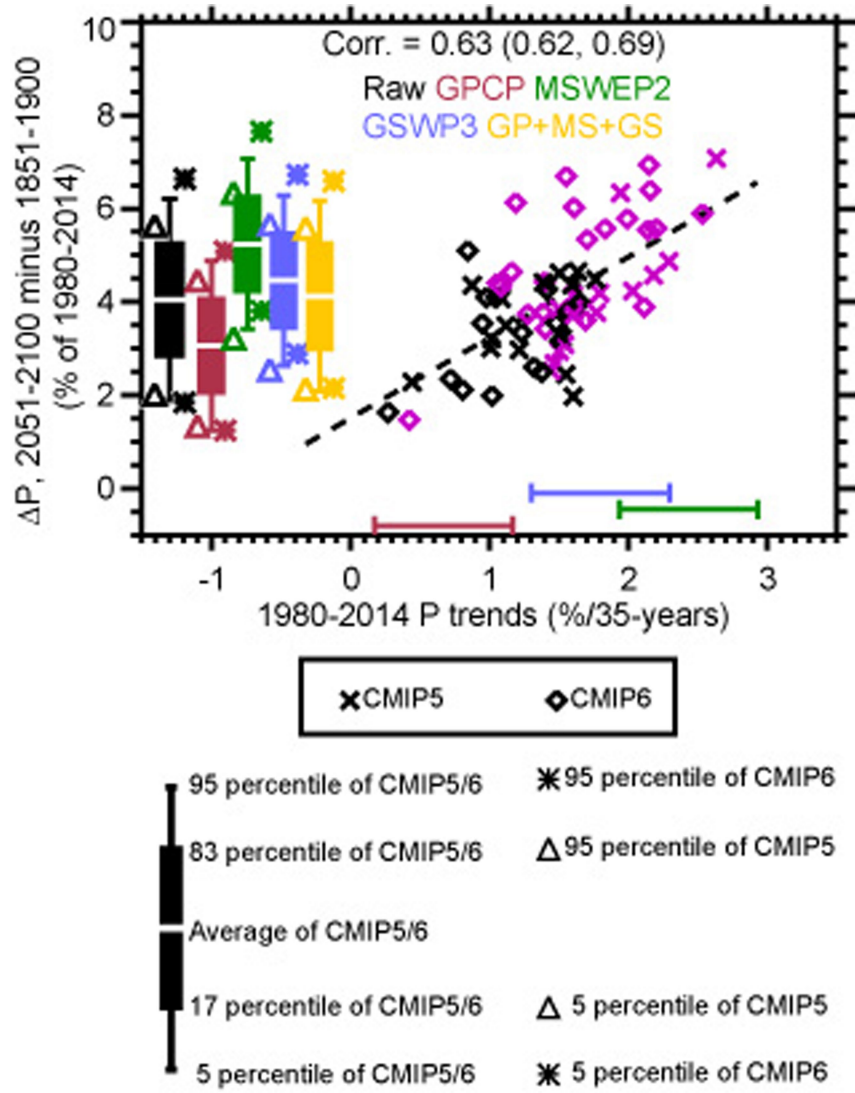
Extended Data Fig. 3 | Observational constraints on the future ΔP using only CMIP5 or CMIP6. Horizontal axes show the recent past (1980–2014) trends of (top) T ($^{\circ}\text{C}$ per 35 yr) and (bottom) P^* (% per 35 yr) for (left) CMIP5 and (right) CMIP6. Vertical axes indicate the future ΔP (2051–2100 minus 1851–1900 of hist+4.5, % of the 1980–2014 mean values). P^* indicates precipitation averaged over the world except for some tropical land regions with few rain gauge observations (Extended Data Fig. 2b). Crosses and diamonds are CMIP5 and CMIP6 ESMs (ensemble mean for each ESM), respectively. Purple crosses/diamonds denote the ESMs whose recent past T trends are higher than the

upper bound of HadCRUT4. Pearson's correlations of the ESMs are denoted in the panels. Those correlations are significant at the 5% level. Dashed lines show the linear regressions. Horizontal bars indicate the 5–95% ranges of HadCRUT4 (light blue), GISTEMP4 (light green), GPCP (red), MSWEP2 (green) and GSWP3 (blue) (Methods). Box plots show the average (white line), 17–83% range (box), and 5–95% range (vertical bar) for the raw ESMs (black) and the constrained ranges using the observations (colours; navy and yellow for Had+GIS and GP+MS+GS, respectively).



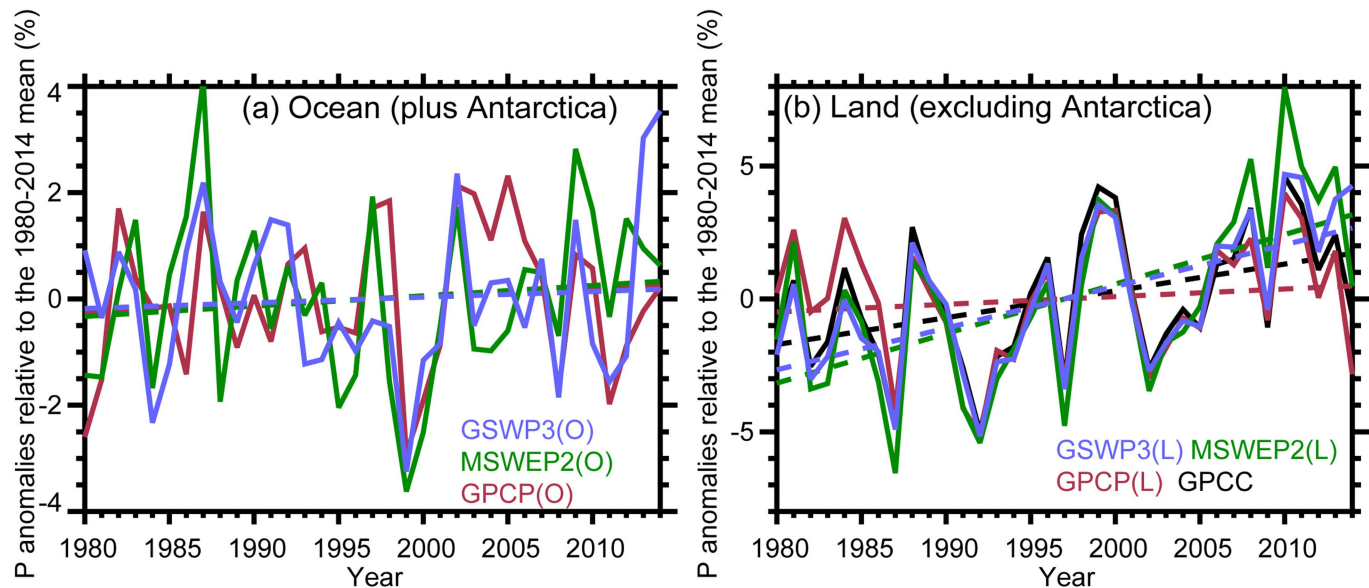
Extended Data Fig. 4 | Past trends of P due to individual and all forcing factors. (a) Long-term (left, 1851–2014, % per 164 yr) and recent (right, 1980–2014, % per 35 yr) past trends of P in the ensembles of hist-GHG (red), hist-aer (blue) and hist-nat (green). (b) Horizontal and vertical axes are the long-term

past trends of P (% per 164 yr) in hist+4.5 and hist-GHG, respectively.
(c) Horizontal and vertical axes are the recent past trends of P (% per 35 yr) in hist+4.5 and hist-GHG, respectively.



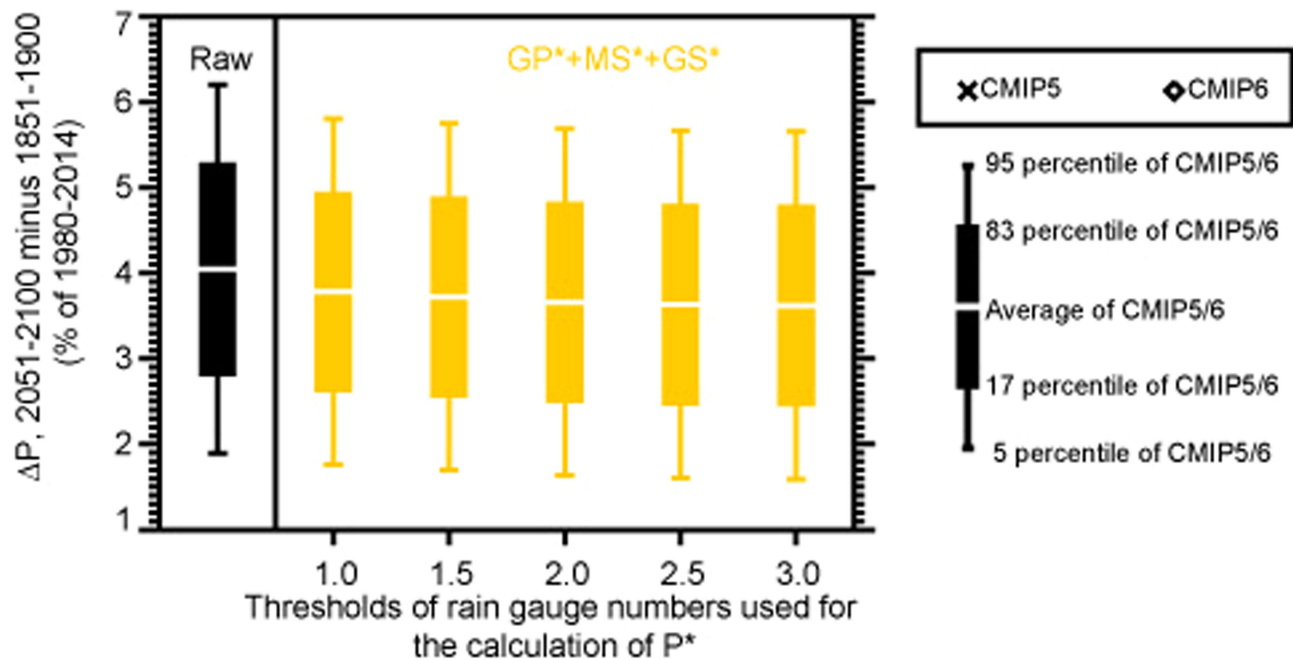
Extended Data Fig. 5 | Observational constraints on the future ΔP using historical P trend. Vertical axis indicates the future ΔP (2051–2100 minus 1851–1900 of hist+4.5, % of the 1980–2014 mean values). Horizontal axis shows the recent past (1980–2014) trends of P (% per 35 yr). Crosses and diamonds are CMIP5 and CMIP6 ESMs (ensemble mean for each ESM), respectively. Purple crosses/diamonds denote the ESMs whose recent past T trends are higher than the upper bound of HadCRUT4. Dashed line shows the linear regression. Horizontal bars indicate the 5–95% ranges of GPCP (red), MSWEP2 (green) and

GSWP3 (blue) (see Methods). Box plots show the average (white line), 17–83% range (box), and 5–95% range (vertical bar) for the raw CMIP5 and CMIP6 ESMs (black) and the constrained ranges using the observations (colours; yellow for GP+MS+GS). Triangle and asterisk symbols denote the 5–95% ranges using only the CMIP5 or CMIP6 ESMs, respectively. Pearson's correlations of the CMIP5 and CMIP6 ESMs are denoted in the panel. Those correlations are significant at the 5% level.



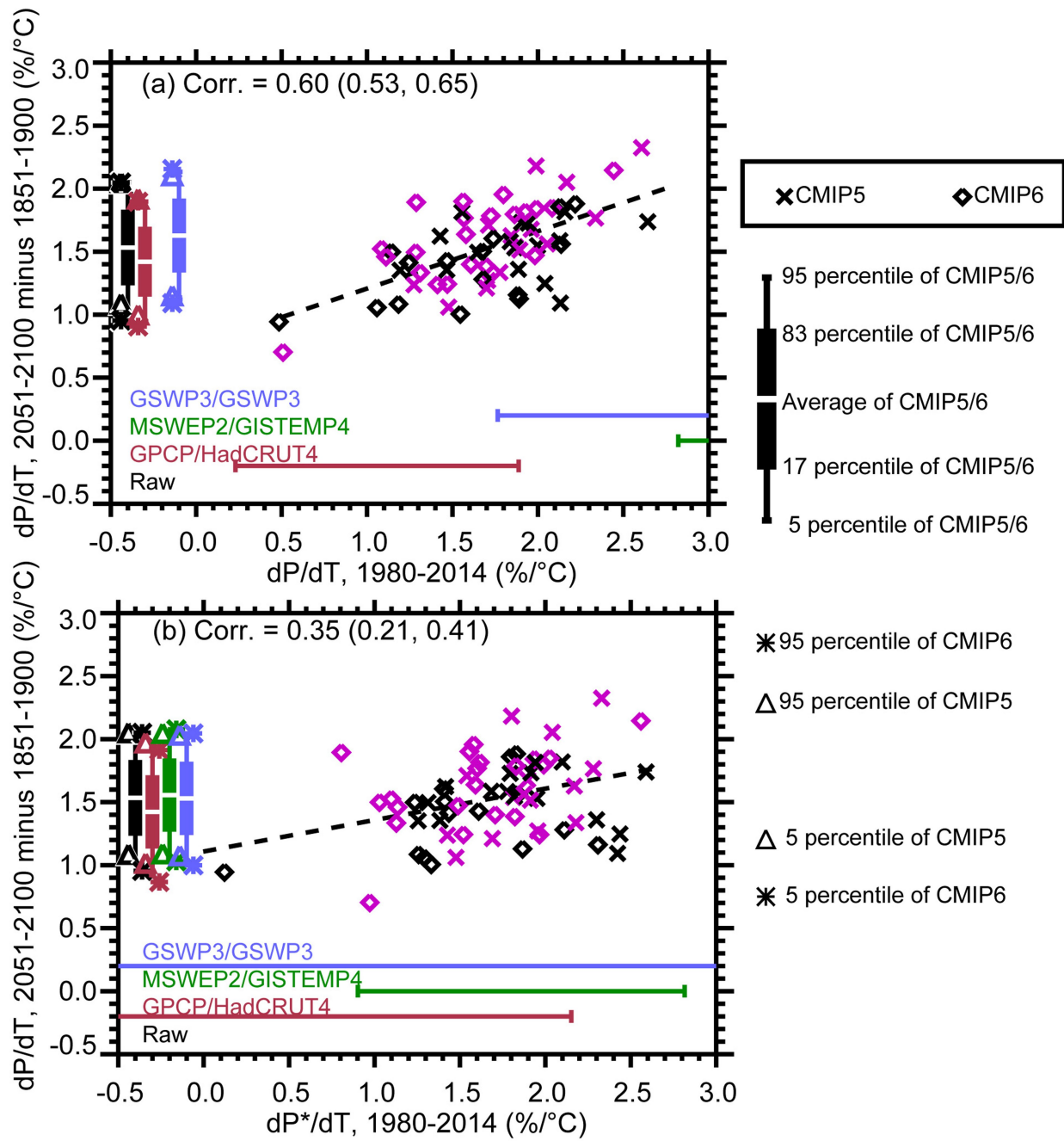
Extended Data Fig. 6 | Discrepancies between observed precipitation datasets over the ocean and land. Solid lines indicate the time series of precipitation anomalies relative to the 1980–2014 mean (%) averaged over (a)

the ocean area plus Antarctica and (b) the land area except for Antarctica. Dashed lines show the linear trends. Red, green, blue and black (only for (b)) lines are GPCP, MSWEP2, GSWP3 and GPCC, respectively.



Extended Data Fig. 7 | Effects of difference in the P^* definition on the constraints. Vertical axes indicate the future ΔP (2051–2100 minus 1851–1900 of hist+4.5, % of the 1980–2014 mean values) of the CMIP5 and CMIP6 ESMs. Box plots show the average (white line), 17–83% range (box), and 5–95% range

(vertical bar) for the raw CMIP5/6 ESMs (black) and the constrained ranges using the P^* trends of GP+MS+GS (yellow). The horizontal axis indicates the thresholds of rain gauge numbers used for the calculation of P^* .



Extended Data Fig. 8 | Relationships between past and future dP/dT (% per ${}^\circ\text{C}$). Vertical axes indicate the future dP/dT (calculated by dividing ΔP by ΔT of ‘2051–2100 minus 1851–1900’). Horizontal axes show the recent past (a) dP/dT and (b) dP^*/dT (calculated by dividing the 1980–2014 trends of P and P^* by the 1980–2014 T trends). Pearson’s correlations of the CMIP5 and CMIP6 ESMs are denoted in the panels. Those correlations are significant at the 5% level except for the CMIP5 of (b). Horizontal bars indicate the 5–95% ranges of GPCP (red),

MSWEP2 (green) and GSWP3 (blue). Box plots show the average (white line), 17–83% range (box), and 5–95% range (vertical bar) for the raw CMIP5 and CMIP6 ESMs (black) and the constrained ranges using observations (colours). Because all the CMIP5 and CMIP6 ESMs are out of the range of MSWEP2/GISTEMP4 in (a), the corresponding constrained range is not available. Triangle and asterisk symbols denote the 5–95% ranges using only the CMIP5 or CMIP6 ESMs, respectively.

Extended Data Table 1 | The analysed CMIP6 (left) and CMIP5 (right) ESMs and their ensemble sizes

CMIP6							CMIP5					
	Model name	hist+4.5	hist+2.6	hist+8.5	hist-GHG	hist-aer	hist-nat		Model name	hist+4.5	hist+2.6	hist+8.5
1	ACCESS-CM2	3	3	3	0	0	0	37	ACCESS1-0	1	0	1
2	ACCESS-ESM1-5	10	10	10	0	0	0	38	ACCESS1-3	1	0	1
3	AWI-CM-1-1-MR	1	1	1	0	0	0	39	BNU-ESM	1	1	1
4	BCC-CSM2-MR	1	1	1	3	3	3	40	CCSM4	6	6	6
5	CESM2	5	4	4	0	0	0	41	CESM1-BGC	1	0	1
6	CESM2-WACCM*	3	1	3	0	0	0	42	CESM1-CAM5*	3	3	3
7	CMCC-CM2-SR5	1	1	1	0	0	0	43	CMCC-CM*	1	0	1
8	CNRM-CM6-1	6	6	6	10	10	10	44	CMCC-CMS	1	0	1
9	CNRM-CM6-1-HR*	1	1	1	0	0	0	45	CNRM-CM5	1	1	5
10	CNRM-ESM2-1	8	4	5	0	0	0	46	CSIRO-Mk3-6-0	10	10	10
11	CanESM5	25	10	10	16	12	10	47	CSIRO-Mk3L-1-2	3	0	0
12	EC-Earth3	17	7	8	0	0	0	48	CanESM2	5	5	5
13	EC-Earth3-CC*	1	0	1	0	0	0	49	EC-EARTH*	4	2	4
14	EC-Earth3-Veg	6	5	5	0	0	0	50	GISS-E2-H	15	3	5
15	EC-Earth3-Veg-LR	3	3	3	0	0	0	51	GISS-E2-H-CC*	1	0	1
16	FGOALS-f3-L	1	1	1	0	0	0	52	GISS-E2-R	16	2	4
17	FIO-ESM-2-0*	3	3	3	0	0	0	53	GISS-E2-R-CC*	1	0	1
18	GFDL-CM4	1	0	1	0	0	0	54	IPSL-CM5A-LR	4	4	4
19	GFDL-ESM4	3	1	1	1	1	3	55	IPSL-CM5A-MR*	1	1	1
20	GISS-E2-1-G	13	1	1	0	0	0	56	IPSL-CM5B-LR*	1	0	1
21	HadGEM3-GC31-LL	1	1	4	4	4	4	57	MIROC-ESM	1	1	1
22	INM-CM4-8	1	1	1	0	0	0	58	MIROC-ESM-	1	1	1
23	INM-CM5-0	1	1	1	0	0	0	59	CHEM*	1	1	1
24	IPSL-CM6A-LR	11	5	5	10	10	10	60	MIROC5	3	3	3
25	KACE-1-0-G*	3	3	3	0	0	0	61	MPI-ESM-LR	3	3	3
26	MCM-UA-1-0	1	1	1	0	0	0	62	MPI-ESM-MR	3	1	1
27	MIROC-ES2L	9	9	9	0	0	0	63	MRI-CGCM3	1	1	1
28	MIROC6	3	10	10	3	3	3	64	NorESM1-M	1	1	1
29	MPI-ESM1-2-HR	2	2	2	0	0	0	65	NorESM1-ME*	1	1	1
30	MPI-ESM1-2-LR	10	10	10	0	0	0	66	bcc-csm1-1	1	1	1
31	MRI-ESM2-0	1	1	2	3	3	3	67	bcc-csm1-1-m*	1	1	1
32	NESM3	2	2	2	0	0	0		inmcm4	1	0	1
33	NorESM2-LM	2	0	0	3	0	0					
34	NorESM2-MM	2	1	1	0	0	0					
35	TaiESM1	1	1	1	0	0	0					
36	UKESM1-0-LL	5	7	5	0	0	0					

Asterisks indicate that these models' 500-year outputs of the piControl runs were not available when we collected the data.

Article

Extended Data Table 2 | The mean values and the constrained 5–95% ranges of the future ΔP (2051–2100 minus 1851–1900, % of 1980–2014)

	hist+2.6 3.4, 1.5–5.3% (raw mean and range)	hist+4.5 4.0, 1.9–6.2%	hist+8.5 5.7, 2.7–8.6%
1980–2019	r = 0.68(T) & 0.71(P) 2.6, 1.1–4.2[34%] 2.8, 1.3–4.3[34%] 2.7, 1.2–4.3[34%] 2.1, 0.6–3.6[39%]	r= 0.61(T) & 0.73(P) 3.4, 1.6–5.3[27%] 3.6, 1.8–5.4[27%] 3.5, 1.7–5.4[27%] 2.7, 1.0–4.4[40%]	r= 0.59(T), 0.72 (P) 4.7, 2.2–7.3[25%] 5.0, 2.4–7.5[25%] 4.9, 2.3–7.4[24%] 3.7, 1.4–6.0[39%]
1980–2014	r = 0.62(T), 0.54(P) & 0.39 (P*) HadCRUT4 GISTEMP4 Had+GIS GPCP MSWEP2 GSWP3 GP+MS+GS GPCP* MSWEP2* GSWP3* GP*+MS*+GS*	r= 0.60(T), 0.63(P) & 0.49(P*) 2.7, 1.0–4.3[27%] 2.7, 1.1–4.3[27%] 2.7, 1.1–4.3[27%] 2.6, 0.9–4.3[22%] 4.2, 2.5–5.9[22%]+ 3.6, 2.0–5.3[22%]+ 3.4, 1.6–5.2[9%] 2.8,1.0–4.7[9%] 3.2,1.4–5.0[9%] 3.0,1.2–4.9[9%] 3.1,1.3–4.9[8%]	Rr=0.56(T), 0.63(P) & 0.43(P*) 4.8, 2.1–7.4[20%] 4.8, 2.2–7.4[20%] 4.8, 2.2–7.4[20%] 4.3, 1.8–6.8[28%] 7.2, 4.7–9.7[28%]+ 6.2, 3.7–8.7[28%]+ 5.8, 3.0–8.5[11%] 4.8,2.0–7.6[10%] 5.4,2.6–8.2[10%] 5.1,2.3–7.9[10%] 5.2,2.4–8.0[9%]
1985–2019	r = 0.69(T) & 0.77 (P) HadCRUT4 GISTEMP4 Had+GIS GPCP	r= 0.62(T) & 0.74(P) 2.6, 1.1–4.2[35%] 2.9, 1.3–4.4[35%] 2.8, 1.2–4.3[34%] 2.3, 0.9–3.7[45%]	r = 0.58 (T) & 0.72 (P) 4.7, 2.2–7.3[24%] 5.1, 2.5–7.6[24%] 4.9, 2.3–7.5[23%] 4.1, 1.8–6.4[40%]
1985–2014	r = 0.64(T), 0.62(P) & 0.54(P*) HadCRUT4 GISTEMP4 Had+GIS GPCP MSWEP2 GSWP3 GP+MS+GS GPCP* MSWEP2* GSWP3* GP*+MS*+GS*	r = 0.61(T), 0.65(P) & 0.57(P*) 2.6, 1.0–4.2[28%] 2.7, 1.1–4.3[28%] 2.7, 1.1–4.3[28%] 2.7, 1.1–4.4[28%] 4.4, 2.8–6.0[28%]+ 3.9, 2.3–5.5[28%]+ 3.5, 1.7–5.3[12%]+ 2.5,0.8–4.3[18%] 3.0,1.3–4.7[18%] 3.0,1.3–4.8[18%] 2.9,1.2–4.7[15%]	r = 0.56(T), 0.65(P) & 0.52(P*) 4.7, 2.1–7.4[20%] 4.9, 2.2–7.5[20%] 4.8, 2.2–7.4[20%] 4.6, 2.2–7.1[30%] 7.4, 4.9–9.8[30%]+ 6.5, 4.1–9.0[30%]+ 5.9, 3.1–8.6[13%]+ 4.5,1.8–7.2[16%] 5.1,2.4–7.8[16%] 5.2,2.5–7.9[16%] 5.1,2.3–7.8[13%]
1975–2019	r= 0.69 (T) HadCRUT4 GISTEMP4 Had+GIS	r = 0.63 (T) 3.6, 1.8–5.4[30%] 3.8, 2.0–5.6[30%] 3.7, 1.9–5.5[29%]	r = 0.61 (T) 5.0, 2.5–7.5[27%] 5.2, 2.7–7.7[27%] 5.1, 2.6–7.6[27%]
1970–2019	r= 0.69 (T) HadCRUT4 GISTEMP4 Had+GIS	r = 0.65 (T) 3.6, 1.8–5.4[31%] 3.9, 2.1–5.7[31%] 3.8, 2.0–5.6[30%]	r= 0.63 (T) 5.0, 2.5–7.5[28%] 5.3, 2.8–7.8[28%] 5.2, 2.7–7.7[27%]

Asterisks indicate that those ECs use the historical P^* trends. Note that the GPCP, MSWEP2 and GSWP3 data are available only for 1980–2019, 1980–2016 and 1980–2014, respectively. Plus symbols denote that the constrained upper bound is not lower than that of the raw range. All the Pearson's correlations (r) between the historical trends and future ΔP are significant at the 5% level. Square brackets indicate the relative reduction of variance (%).